Chapter 11
Numerical Simulation of a Synthetic Jet Actuator for Active Flow Control

Marcin Kurowski

11.1 Introduction

Aerodynamic properties have been widely enhanced with the use of flow control devices in the engineering applications, e.g., airplanes, helicopters, and wind turbine rotors (Casalino et al. 2008; Yen and Ahmed 2013) for many years. Flow separation or transition point control can be done by passive methods which do not require any additional power supply (Gurney Flaps, vortex generators, airfoil shape modification) (Bechert et al. 2000; Shan et al. 2008) or using active devices with an additional energy input (steady blowing, synthetic jet actuators) (Gul et al. 2014). In fluid dynamics, a synthetic jet flow is a jet flow synthesized from an ambient fluid where the stream of the fluid mixes with the surrounding medium. This can be generated using an electromagnetic, piezoelectric, or mechanical driver. The synthetic jet fluid motion is obtained by an alternate suction and ejection of fluid through an orifice or a slot bounding a small cavity. This is generated by a time periodic oscillation of a diaphragm built into the cavity wall. Oscillation of the membrane is a response of the piezoelectric material to the applied voltage. During the oscillation cycle, the cavity volume alternately decreases the expelling fluid during the blowing cycle and increases the cavity volume drawing in fluid during the suction cycle. A membrane can be perpendicular or parallel to the surface in which a hole or a slot is introduced. The scheme of the synthetic jet actuator with perpendicular and parallel membranes is presented in Fig. 11.1.

M. Kurowski (✉)
Institute of Fluid-Flow Machinery, Polish Academy of Sciences, Gdansk, Poland
e-mail: marcin.kurowski@imp.gda.pl

P. Doerffer et al. (eds.), *Recent Progress in Flow Control for Practical Flows*,
DOI 10.1007/978-3-319-50568-8_11

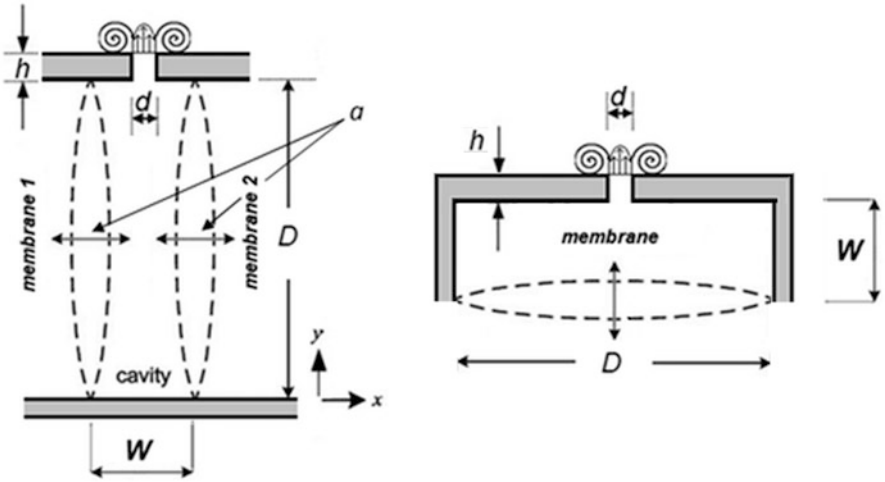

Fig. 11.1 Scheme of the synthetic jet actuator with perpendicular and parallel membranes

Many studies of the synthetic jet have been performed using simplified actuator models:

- The boundary condition at the orifice exit (the wall-normal velocity profile) (Lee and Goldstein 2002; Mallinson et al. 2001)
- The moving piston condition (Fugal et al. 2005)

The numerical modeling of the synthetic jet actuator is described in the following sections.

11.2 Initial and Updated Synthetic Jet Models

This section describes numerical simulation details of initial and updated synthetic jet models. Computational fluid dynamic (CFD) software, turbulence model used in simulation, and other simulation parameters are described. Moving–Deforming-Mesh method used for the two-dimensional (2D) CFD vibrating diaphragm simulation is presented in this section as well.

Commercial package ANSYS Fluent is used for 2D and 3D CFD simulations. Equations of conservation of mass and momentum are solved during the simulation for compressible flow. Compressibility effects have to be taken into account because of the change of the density as a result of moving diaphragm.

One can distinguish two major sections of the proposed geometry. The first region is the ambient air outside the actuator where the jet is developed and the second region includes synthetic jet actuator cavity. Ambient air and cavity are connected through a duct. The ambient air boundary conditions are specified as a pressure outlet, while all the surfaces are considered as walls.

Ambient air region is meshed with structured mesh, as well as the duct and central part of the synthetic jet actuator cavity. In cavity regions adjacent to the moving walls, a tri-pave unstructured mesh has to be used to allow membrane node displacement during the simulation. Unstructured mesh in the deforming zone is a requirement of the Moving–Deforming-Mesh feature in the software (described later). This approach allows to reduce the number of re-meshing nodes during every time step. Combination of the structured and unstructured mesh significantly reduces size of the model and as a result reduces the needed computational power and simulation time.

The shear stress transport (SST) k-ω turbulence model (Menter 1994) is a two-equation eddy-viscosity model which has been proven to be very effective in similar applications. The use of a k-ω formulation in the inner parts of the boundary layer makes the model directly usable all the way down to the wall through the viscous sub-layer; hence, the SST k-ω model can be used as a low-Re turbulence model without any extra damping functions. The SST formulation also switches to a k-ε behavior in the free stream.

By default, ANSYS Fluent updates the node positions on a dynamic zone by applying the solid-body motion equation. This implies that there is no relative motion between the nodes on the dynamic zone. However, if there is a need to control the motion of each node independently, the user-defined function DEFINE_GRID_MOTION can be used. A mesh motion UDF can, for example, update the position of each node based on the deflection due to fluid–structure interaction. Improved synthetic jet actuator model with Moving–Deforming Mesh (MDM) allows to replace surface boundary condition with deforming wall. Membrane deformation profile from finite element model can be imported as an input to CFD simulation. MDM makes possible to simulate flow in the cavity and capture the real physical phenomenon.

Initial membrane deformation profile has been written using formula:

$$y = A \ \sin(2\pi ft) \sin\left[\pi\left(\frac{x-l}{D}\right)\right] \tag{11.1}$$

Updated deformation profile of moving membrane used in the further simulations is given by formula

$$y = A \ \sin(2\pi ft)\left[1-\left(\frac{x}{r}\right)^2\right]^2 \tag{11.2}$$

where x is membrane displacement in x-direction [m], A is displacement amplitude [m], f is forcing frequency [Hz]. t is time [s], y is y-axis coordinate, l is the distance from inlet to the actuator [m], and r is membrane radius [m].

The membrane is clamped to the chamber on the edge. Equation 11.2 describes deformation of the membrane in the area close to the wall (effect of clamp) in a more realistic method than Eq. (11.1) as it is shown in Fig. 11.2.

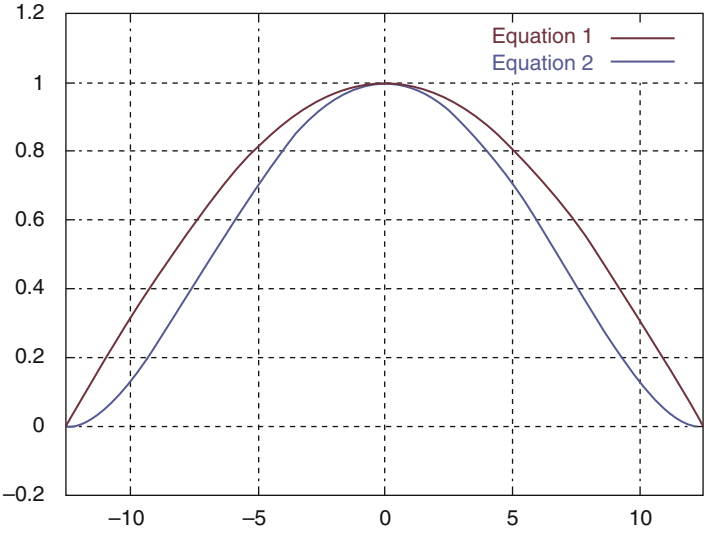

Fig. 11.2 *Red line*—plot of initial equation, *blue line*—plot of updated equation of membrane deformation

A lot of studies of the synthetic jet have been performed using simplified model of the actuator. One of the methods is based on the boundary condition at the orifice exit (the wall-normal velocity profile). Another method of representing the synthetic jet behavior is a moving piston condition. One has to notice that only the moving–deforming membrane boundary condition provides the most accurate physical phenomenon. On the other hand, use of the re-meshing method for every time step requires a lot of computational power and is time-consuming.

11.3 Shape Optimization

Velocity magnitude vectors in the blowing cycle are presented in Fig. 11.3 for initial model with straight edges. Vortices created at the orifice exit are visible.

Simulation results show reversed flow in the duct during blowing cycle which affects flow velocity on the actuator exit; therefore, duct shape has been investigated. Duct edge inclination 45° and corresponding velocity vectors are presented in Fig. 11.4. Duct edge inclination 60° and corresponding velocity vectors are presented in Fig. 11.5. Rounded duct edge and jet velocity vectors are presented in Fig. 11.6.

The best simulation results are obtained for the actuator with rounded edges. Separation area and reversed flow in the duct are minimized compared to actuator with inclined edges. Actuator geometry has been defined in the meaning of membrane diameter, orifice diameter, and actuator height and is presented in Table 11.1.

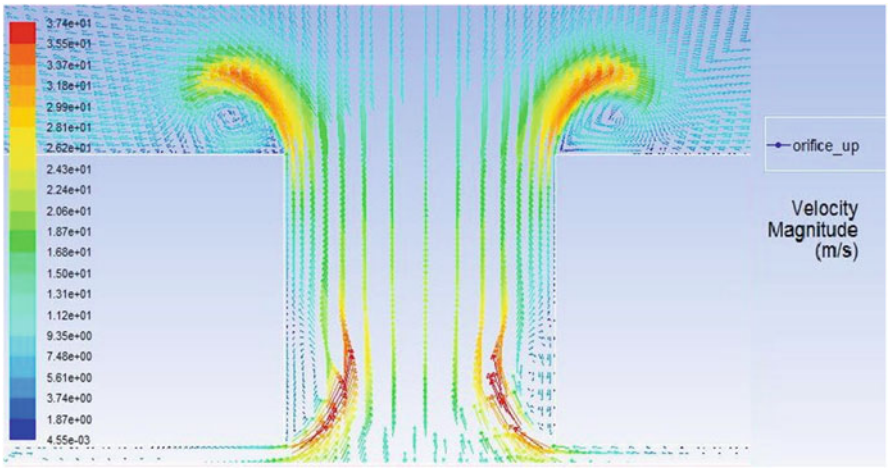

Fig. 11.3 Vectors of the velocity magnitude during the blowing cycle, initial model with straight edges

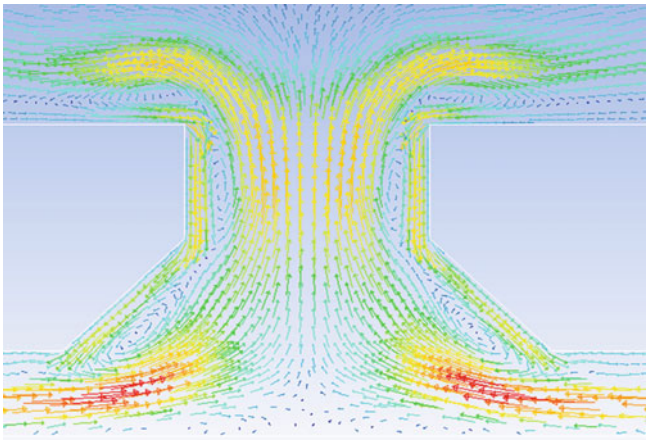

Fig. 11.4 Duct geometry with 45° edge inclination—vectors of the jet velocity magnitude

Scheme of the actuator with one and with two perpendicular membranes in cavity is presented in Fig. 11.7.

11.4 Parametric Study

There is a need to study the effect of synthetic jet individual parameters for synthetic jet flow maximization. A parametric study was carried out to find the optimal parameters. Numerical simulations of the actuator for various membrane amplitudes and different forcing frequencies were conducted. All the simulations were

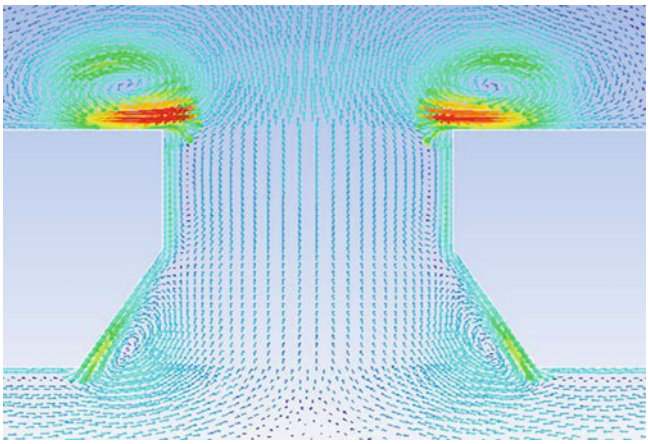

Fig. 11.5 Duct geometry with 60° edge inclination—vectors of the jet velocity magnitude

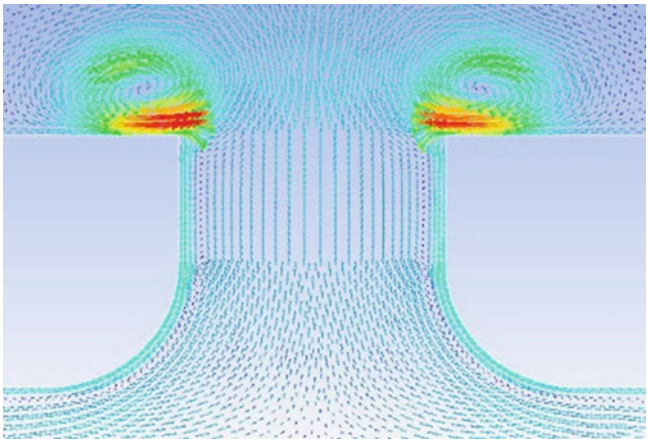

Fig. 11.6 Duct geometry with rounded edge (radius 0.5 mm)—vectors of the jet velocity magnitude

performed for two cases—for one membrane in a cavity and for two membranes in a cavity (Fig. 11.7). The influence of the vibrating membrane amplitude on the jet velocity was investigated varying the peak-to-peak displacement of the diaphragm from $a = 2e10^{-5}$ m to $a = 1e10^{-4}$ m. As the displacement amplitude increased, the change of the cavity volume increased during the cycle as well. As a result, more fluid was forced to exit the actuator during the blowing phase. It was decided to undertake a numerical simulation of an oscillating membrane in a wide range of displacement values to maximize the jet velocity. One has to keep in mind the fact that piezoelectric membrane displacement is a function of the applied voltage; therefore, the power consumption during the actuator operation can be an issue.

Table 11.1 Actuator geometry parameters

Membrane diameter D [mm]	Orifice diameter d [mm]	Orifice length h [mm]	Actuator height H [mm]
25.0	1.0	1.0	1.5
			2.0

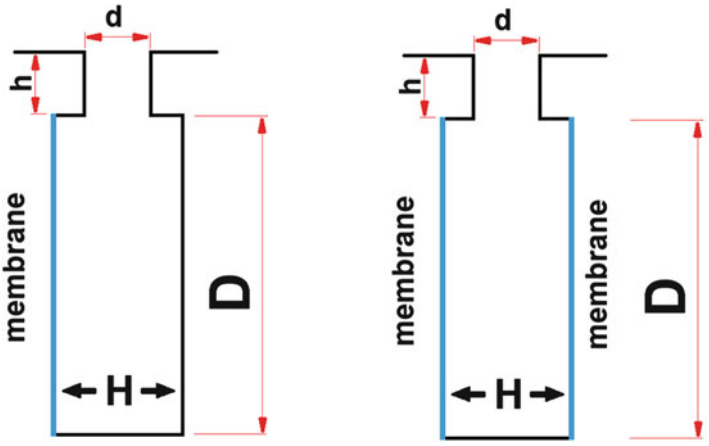

Fig. 11.7 Scheme of the actuator with one (*left*) and with two (*right*) membranes in the cavity

At resonant frequencies, the synthetic jet generator can generate maximum output velocity. The synthetic jet generator should be operated on its resonant frequencies to reduce the power input of energy. A preliminary design of the synthetic jet generator can be made using the lumped element modeling (LEM) (Gallas et al. 2003) method based on the electroacoustic theory. The LEM method is based on an analogy between electrical and acoustic domains. Two main forcing frequencies can be specified in the synthetic jet actuator application. One corresponds to the diaphragm natural frequency, and the other corresponds to the cavity resonant frequency (Helmholtz frequency).

11.4.1 Membrane Structural Resonance

The diaphragm natural frequency (fmem) depends on the material properties, mass, and dimensions of diaphragm. Using the LEM method, the diaphragm natural frequency is given by the expression

$$f_{\text{mem}} = \frac{1}{2\pi}\sqrt{\frac{1}{M_{\text{aD}}C_{\text{aD}}}} \tag{11.3}$$

where M_{aD} is the diaphragm acoustic mass and C_{aD} is the acoustic compliance of a homogeneous clamped circular plate. From the diameter of an oscillating circular membrane in the LEM simulation, the deformation profile is exported and used as the input in the two-dimensional CFD simulations using the MDM method. Based on the LEM method, the membrane natural frequency used in the simulations is $f_{mem} = 740$ Hz.

11.4.2 Helmholtz Frequency

Thinking of the cavity resonance in terms of an oscillating mass of air can give some insight about how the physical properties of the cavity affect the resonant frequency. This can be visualized by the process of pushing extra air into the cavity where overpressure is produced. If the opening to the cavity is larger, the excess air can escape more rapidly to bring the pressure down to external conditions. This leads to a higher cavity resonant frequency. If the neck of the cavity is longer, there is more resistance to the flow of the excess air, and the resonant frequency is lowered. If the cavity volume is increased, then, it takes a greater excess mass of air to produce a given overpressure, and it therefore takes longer for that excess pressure to bring it down to external conditions. The larger cavity will have lower resonant frequency. In general the cavity resonant frequency is given by the expression

$$f_H = \frac{c}{2\pi}\sqrt{\frac{A}{VL}} \tag{11.4}$$

where c is the sound speed (m/s), A is the area of opening (m^2), V is the cavity volume (m^3), and L is the opening length (m). The synthetic jet actuator model parameters used in the presented study are given in Table 11.2.

Simulations were performed for actuator with one membrane and two membranes in the cavity. Results of the vibrating membrane amplitude influence on the jet velocity for one membrane in the cavity are presented in Fig. 11.8. Lines represent velocity magnitude V_{mag} and velocity y-component V_y (in the jet direction)

Table 11.2 Synthetic jet actuator model parameters

Peak-to-peak displacement a [mm]	Membrane diameter D [mm]	Orifice diameter d [mm]	Duct length h [mm]	Actuator height H [mm]		Number of membranes		Forcing frequency [Hz]	
0.02	25	1.0	1.0	1.5	2.0	1	2	740	1650
0.04									
0.06									
0.08									
0.10									

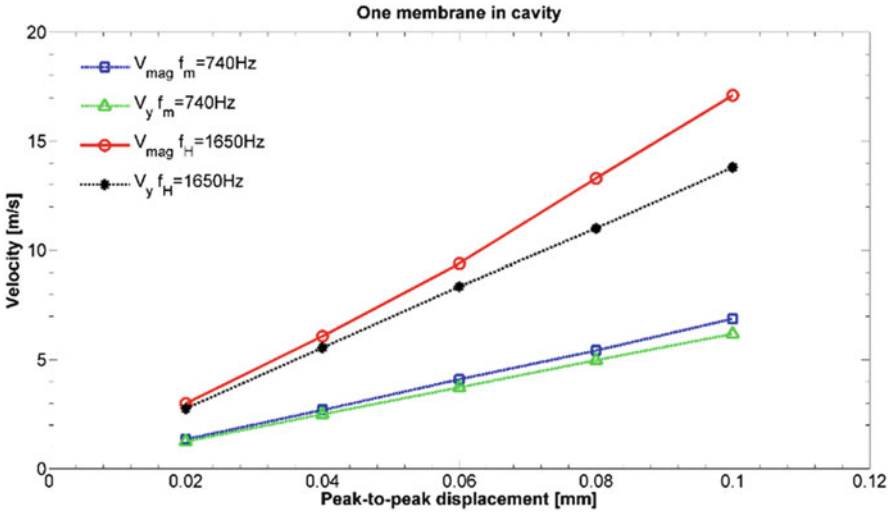

Fig. 11.8 Jet velocity for one membrane in cavity (membrane resonant frequency $f_m = 740$ Hz, cavity resonant frequency $f_H = 1650$ Hz)

for membrane resonant frequency $f_{\text{mem}} = 740$ Hz and cavity resonant frequency $f_{\text{cav}} = 1650$ Hz. All the velocity values are maximum values for the jet during the blowing cycle. Velocity magnitude and velocity y-component are calculated on the actuator exit orifice diameter. Results of the vibrating membrane amplitude influence on the jet velocity for two membranes in cavity are presented in Fig. 11.9. The membranes are actuated in the opposite phase thanks to which the cavity volume is modified twice as much as in the previous case. As it can be observed increase of the membrane displacement results in approximately linear increase of the jet velocity. The higher the membrane amplitude is the higher jet velocity from the actuator can be obtained.

Maximum jet velocities were obtained for membrane displacement $a = 0.1$ mm. For one membrane in cavity, maximum jet velocity was $V = 6.88$ m/s for $f_m = 740$ Hz. For two membranes in cavity, maximum jet velocity was $V = 14.2$ m/s for $f_m = 740$ Hz. For cavity resonant frequency $f_H = 1650$ Hz, maximum jet velocity was $V = 17.1$ m/s for one membrane in cavity and for two membranes $V = 31.5$ m/s. Ratio of jet velocities for actuator arrangement with two membranes to one membrane in cavity is presented in Table 11.3. Use of a second membrane in cavity gives jet velocity two times higher for membrane resonant frequency and for cavity resonant frequency as well.

Flow separation in the duct affects the jet velocity at the actuator exit. This can be observed in the difference between jet velocity magnitude and jet y-direction velocity component presented in Figs. 11.8 and 11.9 for one and two membranes in cavity, respectively.

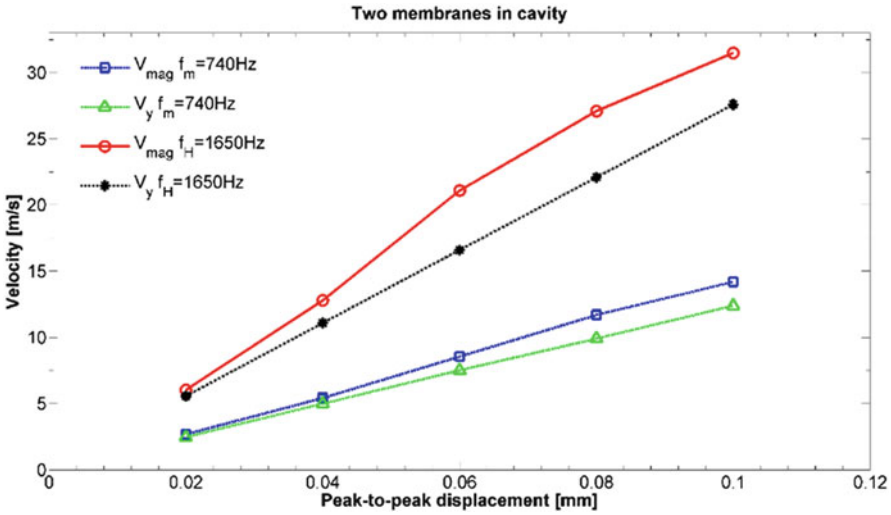

Fig. 11.9 Jet velocity for two membranes in cavity (membrane resonant frequency $f_m = 740$ Hz, cavity resonant frequency $f_H = 1650$ Hz)

Table 11.3 Ratio of jet velocities for actuators with two membranes to one membrane in cavity

	$f_m = 740$ Hz		$f_H = 1650$ Hz	
Peak-to-peak displacement a [mm]	*V*mag	*Vy*	*V*mag	*Vy*
0.02	2.01	1.98	2.02	2.01
0.04	2.02	2.00	2.11	2.00
0.06	2.09	2.02	2.24	1.99
0.08	2.16	1.99	2.04	2.01
0.1	2.06	2.00	1.84	2.00

Contours of velocity magnitude and vortex structure at the actuator exit in the blowing cycle for membrane peak-to-peak displacement $a = 0.06$ mm and one membrane in cavity are presented in Figs. 11.10 and 11.11. Contours of velocity magnitude and vortex structure at the actuator exit in the blowing cycle for membrane peak-to-peak displacement $a = 0.06$ mm and two membranes in cavity are presented in Figs. 11.12 and 11.13. For forcing frequency $f_m = 740$ Hz and actuator with two membranes in cavity, reversed flow area in duct is much larger compared to the case with actuator with one membrane in cavity. This phenomenon can be observed for forcing frequency $f_H = 1650$ Hz as well.

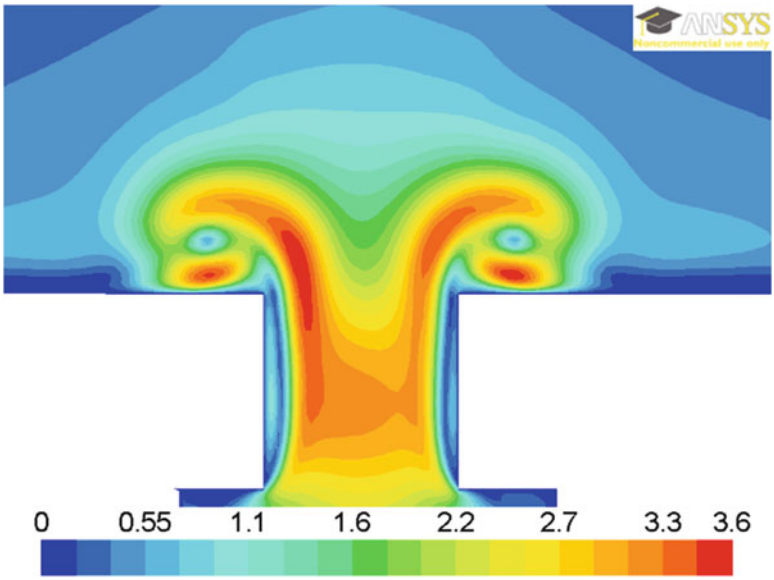

Fig. 11.10 Contours of velocity magnitude in the blowing cycle, one membrane, $f_m = 740$ Hz

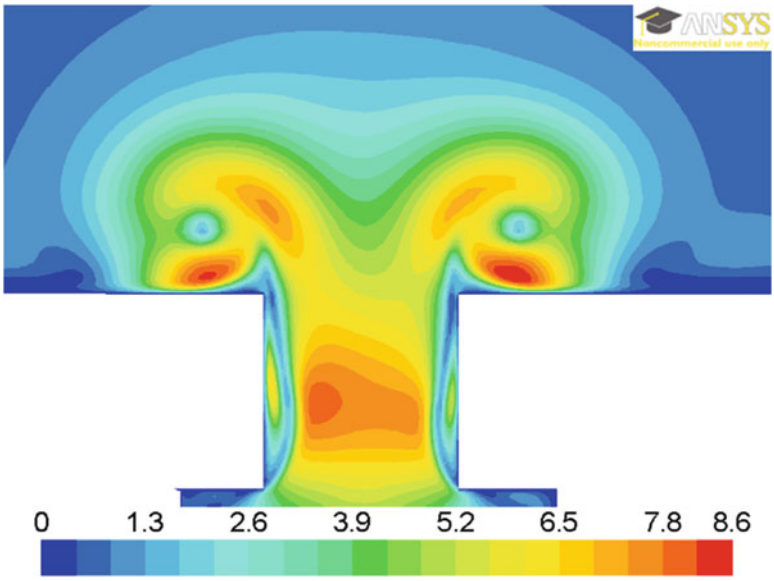

Fig. 11.11 Contours of velocity magnitude in the blowing cycle, one membrane, $f_H = 1650$ Hz

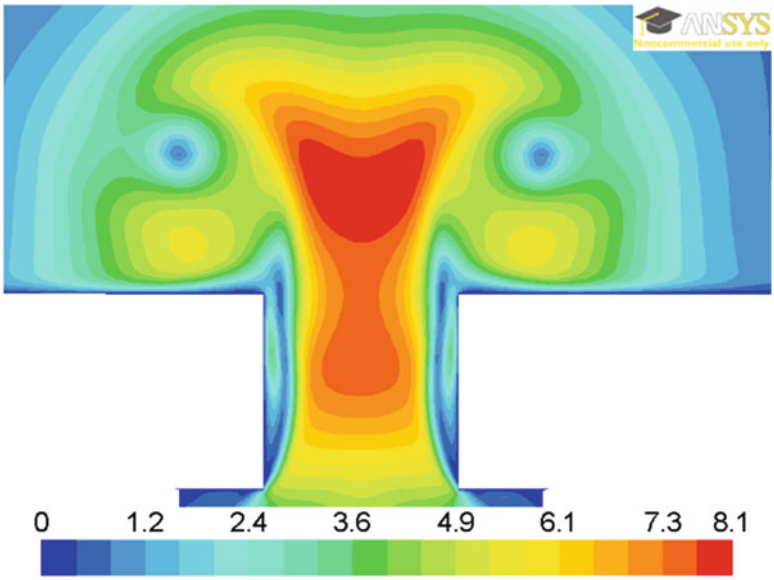

Fig. 11.12 Contours of velocity magnitude in the blowing cycle, two membranes, $f_m = 740$ Hz

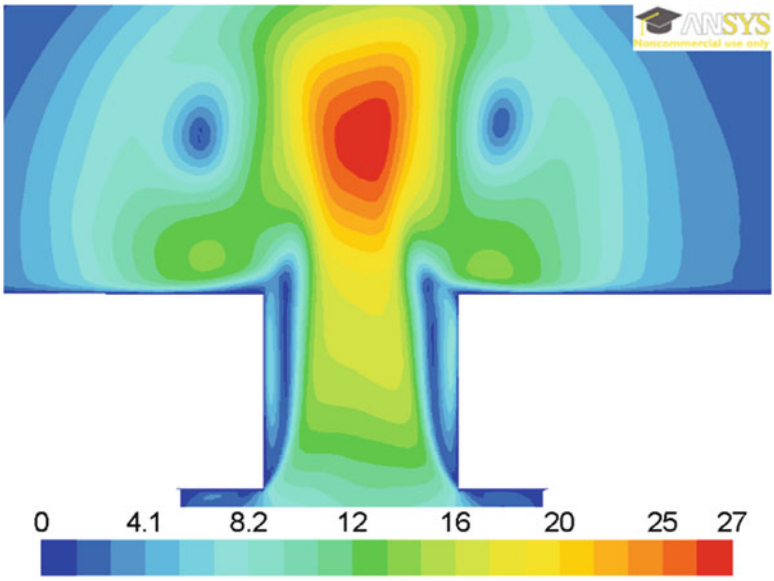

Fig. 11.13 Contours of velocity magnitude in the blowing cycle, two membranes, $f_H = 1650$ Hz

11.5 Bump for Flow Separation

Numerical simulations were performed on a bump implemented into the bottom wall of a wind tunnel section to generate flow separation due to the change of the channel geometry. Scheme of a bump used in numerical simulations is presented in Fig. 11.14.

Bump dimensions are:

- Width—80.0 mm
- Height at the beginning—min. (R_min) = 10.0 mm, max. (R_max) = 29.0 mm
- Height at the end—$r = 7.25$ mm
- Length (Lbump) = 90.0 mm

CFD model of a wind tunnel section with a bump is presented in Fig. 11.15.

Wind tunnel dimensions:

- Height $H = 90.0$ mm
- Width $W = 80.0$ mm
- Length $L = 900.0$ mm

Bump is located 270 mm from the inlet to the wind tunnel. Configurations of a bump height (R) from 10 mm up to 29 mm were investigated in simulations. In every case, radius of a bump in the end was constant $r = 7.25$ mm.

To investigate the flow field over the bump, different velocities on the inlet were applied. Minimal value of velocity in x-direction was 5 m/s, when maximal velocity in x-direction was 20 m/s. Contours of velocity magnitude for some bump geometries are presented below for two cases: inflow velocity 5 m/s and 20 m/s. It can be observed that for bump heights between 29 mm (Fig.11.16) and 20 mm

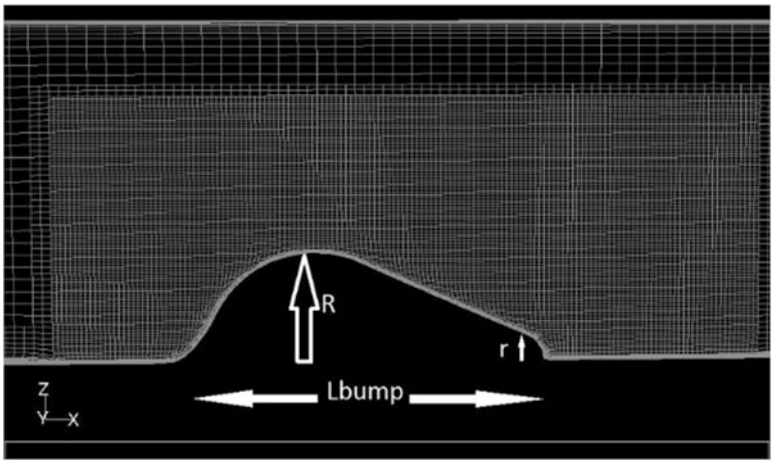

Fig. 11.14 Model of the bump used in CFD simulations

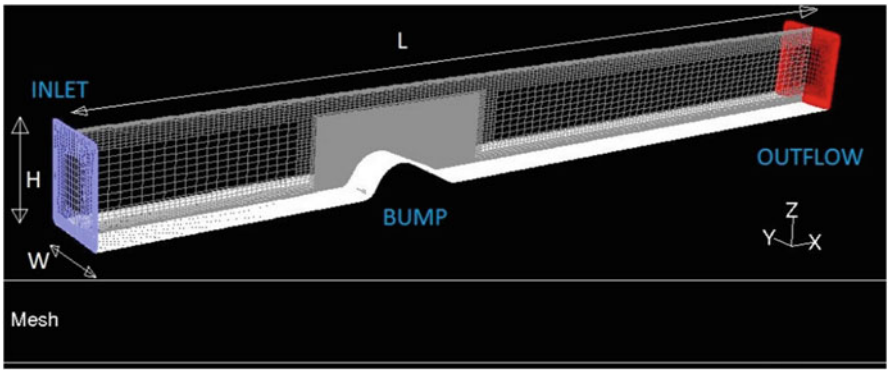

Fig. 11.15 CFD model of a wind tunnel with a bump on the bottom wall

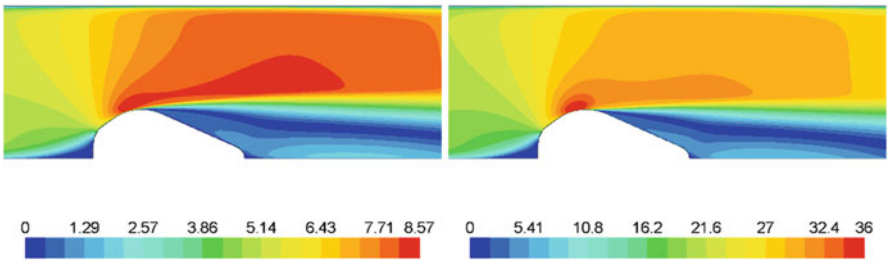

Fig. 11.16 Contours of velocity magnitude, $R = 29$ mm, $V = 5$ m/s (*left*), $V = 20$ m/s (*right*)

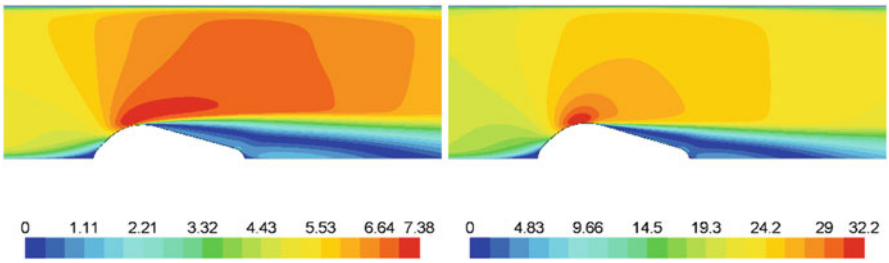

Fig. 11.17 Contours of velocity magnitude, $R = 20$ mm, $V = 5$ m/s (*left*), $V = 20$ m/s (*right*)

(Fig. 11.17), flow separates at the top of the bump. Area of the separated flow is large (indicated by the blue color), and flow is not reattached to the surface of the bump.

Contours of velocity magnitude for bump height 15 mm and inflow velocities 5 m/s and 20 m/s are presented in Fig. 11.18. Separation area is smaller than in previous cases.

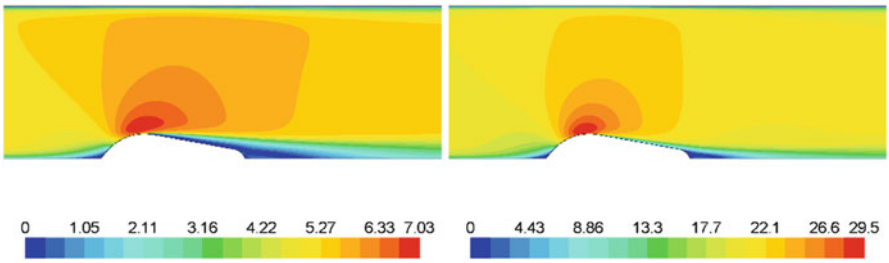

Fig. 11.18 Contours of velocity magnitude, $R = 15$ mm, $V = 5$ m/s (*left*), $V = 20$ m/s (*right*)

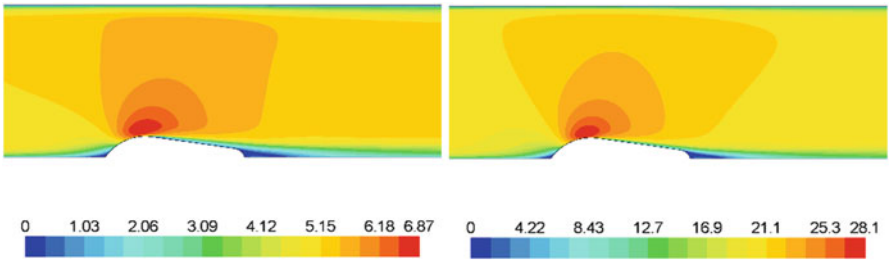

Fig. 11.19 Contours of velocity magnitude, $R = 13$ mm, $V = 5$ m/s (*left*), $V = 20$ m/s (*right*)

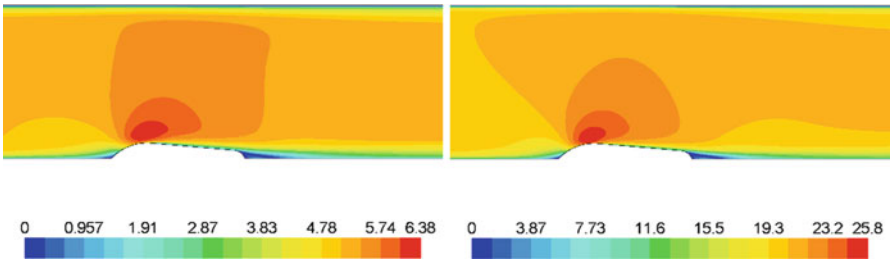

Fig. 11.20 Contoursenlargethispage*-2pc of velocity magnitude, $R = 10$ mm, $V = 5$ m/s (*left*), $V = 20$ m/s (*right*)

For bump height lower than 13 mm there is no flow separation on the bump at all, as it is presented in Figs. 11.19 and 11.20. Flow is attached to the surface of the bump along the whole distance.

Pathlines, colored by velocity magnitude, released from the top of the bump are presented in Fig. 11.21. Bump height is $R = 14$ mm and inflow velocity is 5 m/s. Flow separates on the top of the bump and reattaches to the surface. Separation bubble is clearly visible. In the future simulations, synthetic jet actuators will be placed in front of the separation bubble to investigate possibility to reduce the area of reversed flow.

Contours of velocity magnitude from the cut plane located 1 mm over the bump are presented in Fig. 11.22. Area covered by red color indicates location of the front

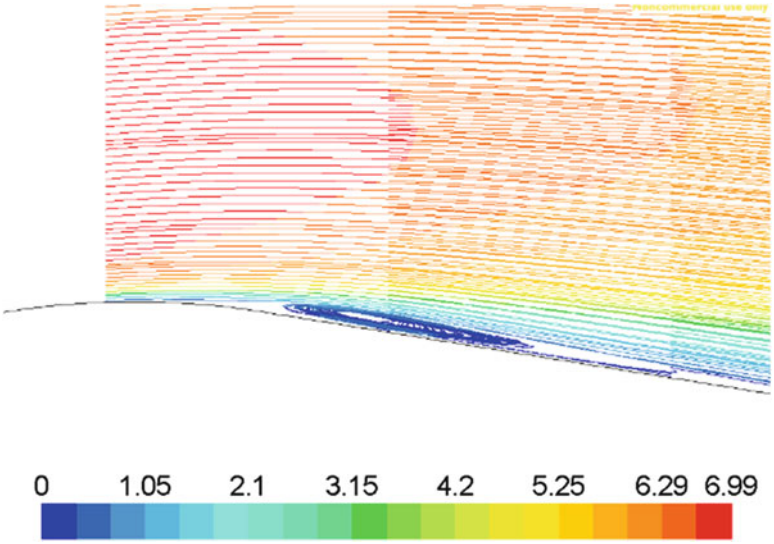

Fig. 11.21 Separation bubble for inflow velocity 5 m/s, bump height $R = 14$ mm

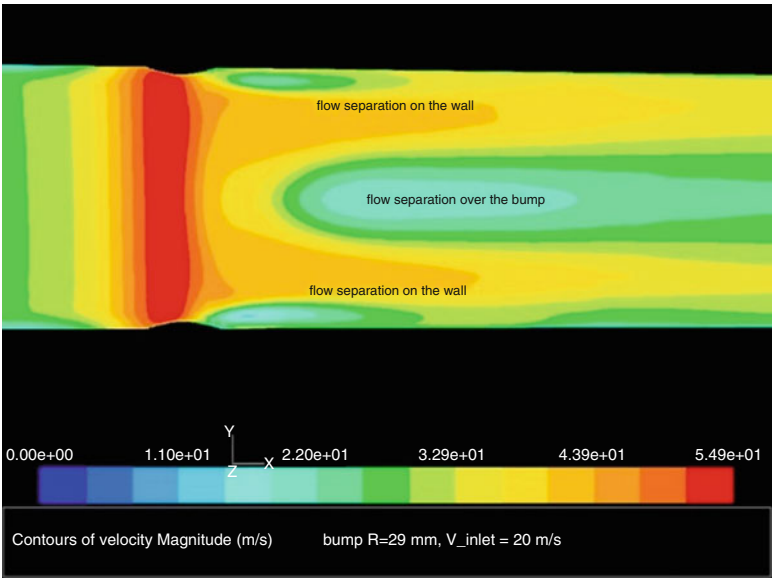

Fig. 11.22 Velocity magnitude contours for bump $R = 29$ mm, inflow velocity 20 m/s, plane cut 1 mm above the bump

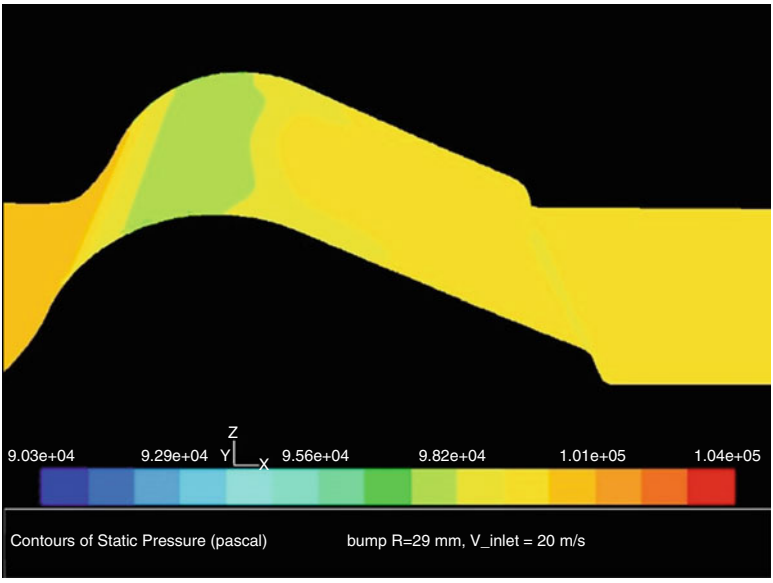

Fig. 11.23 Contours of the static pressure on the bump surface, bump $R = 29$ mm, inflow velocity 20 m/s

part of a bump. In the center of Fig. 11.22, area of lower velocity with respect to the main flow is visible. Separation on the wind tunnel walls is visible in Fig. 11.22 as well.

Contours of the static pressure on the bump surface for bump height in front part 29 mm and inflow velocity 20 m/s are presented in Fig. 11.23.

11.6 Conclusions

This chapter presents a numerical simulation of a synthetic jet actuator using the Moving–Deforming-Mesh method. The synthetic jet actuator is simulated using a membrane perpendicular to the surface arrangement. Investigations of the influence of the membrane amplitude, the forcing frequency, and cavity effect on the jet velocity were carried out, and the results are reported. Two forcing frequencies were used, one of which corresponded to the diaphragm natural frequency, and the other which corresponded to the cavity resonant frequency (Helmholtz frequency). The simulation results show that an increase in the membrane displacement results in an approximately linear increase of the jet velocity. The higher the membrane amplitude, the higher the jet velocity that can be obtained from the actuator. The use of a second membrane in the cavity gives the jet velocity two times higher for the membrane resonant frequency and for the cavity resonant frequency, as well. Maximum jet velocities were obtained for membrane displacement $a = 1\,10^{-4}$ m.

The use of a second membrane in the cavity gives the jet velocity two times higher for the membrane resonant frequency and for the cavity resonant frequency as well. This study was a preliminary study of the synthetic jet actuator for active flow control. The optimization process of the synthetic jet actuator geometry and parameters is ongoing. The numerical results obtained in these investigations are to be validated in the experimental campaign.

Appendix

Code of the user-defined function file used in the 2D synthetic jet actuator numerical simulation with Moving–Deforming-Mesh method is presented below:

```
#include "udf.h"
/* Put proper values in VALUE(variable) places */
#define freq 740     /* forcing frequency, Hz*/
#define amp 0.00008    /* peak-to-peak amplitude, meters     0.00006*/
#define L 0.025 /* chamber's width/membrane's diameter, meters*/
DEFINE_GRID_MOTION(moving_membrane, domain, dt, time, dtime)
{
  Thread *tf = DT_THREAD (dt);
  face_t f;
  Node *node_p;
  real omega, alpha, y, x;
  int n;
/* Set/activate the deforming flag on adjacent cell zone, which     */
/* means that the cells adjacent to the deforming wall will also be */
/* deformed, in order to avoid skewness. */
SET_DEFORMING_THREAD_FLAG (THREAD_T0 (tf));
omega = 2.*M_PI*freq;
alpha = omega * CURRENT_TIME;
begin_f_loop (f, tf)
  {
    f_node_loop (f, tf, n)
      {
        node_p = F_NODE (f, tf, n);
/* Update the current node only if it has not been previously visited: */
    if (NODE_POS_NEED_UPDATE (node_p))
       {
    /* Set flag to indicate that the current node's position has    */
    /* been updated, so that it will not be updated during a future */
    /* pass through the loop: */
NODE_POS_UPDATED (node_p);
y = NODE_Y (node_p);
x = amp*sin(alpha)* ((1-((y-L)/L)*((y-L)/L))*(1-((y-L)/L)*((y-L)/L)));
NODE_X (node_p) = x;
   }
  }
 }
end_f_loop (f, tf);
}
```

References

Bechert DW, Meye R, Hage W (2000) Drag reduction of airfoils with miniflaps. can we learn from dragonflies? In: Fluids 2000 conference and exhibit, Denver, CO, June 19–22, AIAA 2000–2315

Casalino D, Diozzi F, Sannino R, Paonessa A (2008) Aircraft noise reduction technologies: a bibliographic review. Aerosp Sci Technol 12:1–17

Fugal SR, Smith BL, Spall RE (2005) Displacement amplitude scaling of a twodimensional synthetic jet. Phys Fluids 17:045103

Gallas Q, Holman R, Nishida T, Carroll B, Sheplak M, Cattafesta L (2003) Lumped element modeling of piezoelectric-driven synthetic jet actuators. AIAA J 41(2):240–247

Gul M, Uzol O, Akmandor IS (2014) An experimental study on active flow control using synthetic jet actuators over S809 Airfoil. J Phys Conf Ser 524:01210

Lee CY, Goldstein DB (2002) Two-dimensional synthetic jet simulation. AIAA J 40:510

Mallinson SG, Reizes JA, Hong G (2001) An experimental and numerical study of synthetic jet flow. Aeronaut J 105:41

Menter FR (1994) Two-equation eddy-viscosity turbulence models for engineering applications. AIAA J 32(8):1598–1605

Shan H, Jiang L, Liu C et al (2008) Numerical study of passive and active flow separation control over a NACA0012 airfoil. Comput Fluids 37(8):975–992

Yen J, Ahmed NA (2013) Enhancing vertical axis wind turbine by dynamic stall control using synthetic jets. J Wind Eng Ind Aerodyn 114:12–17